Automatic Choroidal Layer Segmentation Using Markov Random Field and Level Set Method

Chuang Wang [iD], Ya Xing Wang, and Yongmin Li [iD]

Abstract—The choroid is an important vascular layer that supplies oxygen and nourishment to the retina. The changes in thickness of the choroid have been hypothesized to relate to a number of retinal diseases in the pathophysiology. In this paper, an automatic method is proposed for segmenting the choroidal layer from macular images by using the level set framework. The three-dimensional nonlinear anisotropic diffusion filter is used to remove all the optical coherence tomography (OCT) imaging artifacts including the speckle noise and to enhance the contrast. The distance regularization and edge constraint terms are embedded into the level set method to avoid the irregular and small regions and keep information about the boundary between the choroid and sclera. Besides, the Markov random field method models the region term into the framework by correlating the single-pixel likelihood function with neighborhood information to compensate for the inhomogeneous texture and avoid the leakage due to the shadows cast by the blood vessels during imaging process. The effectiveness of this method is demonstrated by comparing against other segmentation methods on a dataset with manually labeled ground truth. The results show that our method can successfully and accurately estimate the posterior choroidal boundary.

Index Terms—Choroid layer segmentation, level set method, markov random field, and macular 3D OCT images.

I. INTRODUCTION

THE choroid is an important vascular layer and lies between the retina and the sclera [1], [2]. It contains connective tissues and blood vessels and provides oxygen and nourishment to the retina. The changes of the choroid are important indicators of many eye diseases, in particular glaucoma, high myopia, neovascular and non-neovascular AMD, central serous chorioretinopathy and Vogt-Koyanagi-Harada disease [3]. Therefore, it is important to segment the layers and reconstruct the vascular structure of the choroid and measure the changes of the choroid. Many commercial optical coherence tomography (OCT) imaging systems are now able to capture the 3D choroid images. However, due to the limitations of current imaging technology and the location of the choroid, the boundaries between the choroid and sclera in the images are not apparent in some locations.

It is time consuming or even impossible to manually delineate all the choroidal structures and layers for a large number of images because of the indistinct structures and boundaries in some cases. Therefore, automatic choroidal layer segmentation and reconstruction have attracted many researchers. In this study, we mainly focus on layer segmentation and thickness measurement.

Many automatic or semi-automatic methods [4]–[9] for segmenting the choroidal boundary have been reported recently. Kajie *et al.* [4] presented a statistical model based on the texture and shape to automatically segment the choroid layer from OCT B-scans. Hu *et al.* [5] performed the choroid segmentation semi-automatically by using the graph search algorithm from 3D OCT volumes. Tian *et al.* [6] reported an automatic segmentation method for 2D enhanced depth imaging (EDI) OCT images. The choroidal-sclera interface is located by using the Dijkstra's algorithm. This algorithm is used to find the shortest path for the graph, which is constructed by the valley pixels. Alonson-Caneiro *et al.* [7] developed a dual probability gradient based method to segment the choroid layer automatically from the enhanced OCT B-scans. Danish *et al.* [8] segmented the choroidal boundary using a multi-resolution texture modelled graph cut method from 3D EDI OCT images. Besides, Markov Random Field (MRF) based methods [10]–[12] have been developed for detecting the intra-retinal layers from 2D or 3D OCT images. Rossant *et al.*[10] segmented the Inner layers (Retinal nerve fiber layer (RNFL), Outer Nuclear Layer (ONL), Ganglion Cell Layer(GCL)+Inner Plexiform Layer (IPL), Inner Nuclear Layer (INL)) from macular B-scan by using MRF. Ghorbel *et al.* [11] expanded the MRF method from [10] to segment Inner layers from 3D macular images. Wang *et al.*[12] segmented four layers from 3D optic nerve head image by using Hidden MRF.

Despite these efforts, difficulties remain in segmenting the choroidal layer from macular images, in particular on dealing with indistinct boundaries, shape constraints and region constraints [13] . Fig. 1 shows examples of the challenges.

1) The boundary between the choroid and sclera is not distinct. It is even invisible in some locations as shown in Fig. 1(c), thus the edge based segmentation method cannot accurately segment the layers;
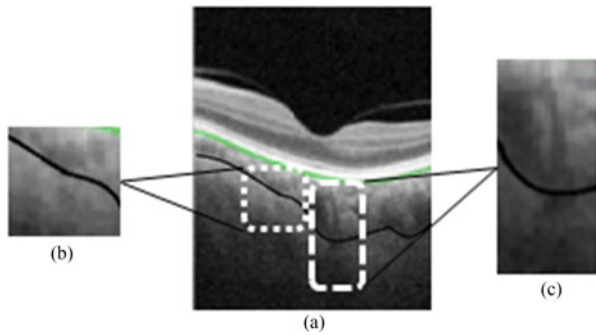
Fig. 1. The challenge of the choroidal layer segmentation. (a) A B-scan from an OCT macular volume image with ground truth marked. (b) The inhomogeneous texture in the choroidal region. (c) The indistinct appearance between the choroid and sclera.

2) It is difficult to locate the choroid by using an intensity based segmentation method because of the inseparable appearance between the choroid and sclera as in Fig. 1(c);

3) The intensity inhomogeneity and the inconsistent texture [Fig. 1(b)] of the choroid makes the region based and texture based segmentation ineffective because of the presence of the blood vessels in the choroid layer.

In order to overcome these difficulties, we present an automatic choroidal layer segmentation method. The baseline of the method is built on the level set framework, with a region term using the Markov Random Field method to model the choroidal layer and sclera, an edge term obtained by calculating the line integral of the edge function and the weighted area of the object region, and a distance regularisation term obtained by computing the contour length of the object region. The following are the key considerations in developing the proposed method:

1) The boundary between the choroid and sclera is visible at some locations of the image. Therefore, the edge information is still important for segmenting the choroid. The edge constraint term is introduced into this method to incorporate the edge information to direct the contour to the desired boundary;

2) We use the Markov Random Field to model the region appearance by incorporating the spatial context of neighbouring pixels. It compensates the intensity inhomogeneity of the choroid and avoids small regions caused by shadows cast by blood vessels. Furthermore, the prior information of the background and choroid is calculated and used to obtain the posterior probability to guide the contour to the desired boundary of the choroid.

3) Finally, the distance regularisation term is used to prevent small and irregular contours appearing during the iterations.

The remainder of this paper is organised as follows. In Section II, the proposed segmentation method is described. The experimental results are presented in Section III. The last section draws the conclusions.

II. METHOD

The choroidal layer is segmented with a typical two-step process, which includes a pre-processing step and a segmentation step. Fig. 2 shows the overview of the automatic choroidal layer segmentation method. At the first step, the 3D anisotropic diffusion method [14] is used to remove the speckle noise and to enhance the contrast between the background and object. We apply the proposed level set method with a region based term, an edge constraint term and a distance regularisation term to locate the choroidal layer boundary at the second step. Finally, the energy functional is minimised by using Partial Differential Equations (PDE).

A. Pre-Processing step

The OCT imaging process often produces speckle noise and imaging artifacts. Fig. 2(a) shows the original 3D macular image, which contains a significant level of speckle noise and artifacts. The conventional anisotropic diffusion approach (Perona-Malik) [14] is used to remove the speckle noise and sharpen the contrast between the choroidal layer and sclera. Fig. 2(e) and (f) show an original B-scan image and the de-noised B-scan image. The nonlinear anisotropic diffusion filter is defined as:

$$\frac{\partial}{\partial t}I(\bar{x}, t) = \text{div}[c(\bar{x}, t)\nabla I(\bar{x}, t)] \tag{1}$$

where the vector $\bar{x}$ represents (x, y, z) and t is the process ordering parameter. $I(\bar{x}, t)$ is macular voxel intensity. $c(\bar{x}, t)$ is he diffusion strength control function, which depends on the magnitude of the gradient of the voxel intensity, and is given by:

$$c(\bar{x}, t) = \exp\left(-\frac{|\nabla I(\bar{x}, t)|^2}{\kappa}\right) \tag{2}$$

where κ is a constant chosen according to the noise level and edge strength, and it was set to 70 in the experiments according to [14]. Finally, the voxel intensities are updated by the following formula:

$$I(t + \triangle t) = I(t) + \triangle t \frac{\partial}{\partial t}I(t) \tag{3}$$

The de-noised image is shown in Fig. 2(b). However, it is impossible to remove all the imaging artifacts by using the de-noising method. In order to reduce the computational complexity and improve the computation efficiency, we cut this image into a small volume by removing all the background information. Fig. 2(c) and (d) show the two chopped volumes. Next, the retinal pigment epithelium boundary, which is normally with strong contrast and can easily be identified, is segmented by using the graph cut method [15]. Then the portion above the retinal pigment epithelium boundary is set to zero to facilitate the segmentation of the posterior choroidal boundary.

At the initialisation stage, we assume the posterior choroidal boundary is in the same shape as the retinal pigment epithelium which is already segmented. A distance displacement of 130 pixels (507 μm) is set between these two boundaries. Let Ω be the image domain, the zero level set of the level set function
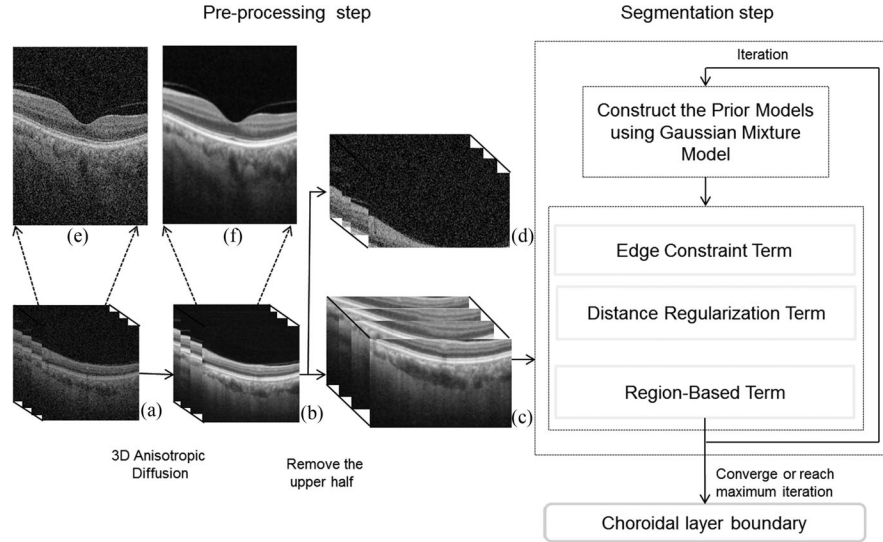
Fig. 2. Block diagram of automatic choroidal layer segmentation. (a) The original macular OCT image. (b) The de-noised OCT image by using the 3D anisotropic diffusion method. (c) and (d) The volume image is cut into two and the upper half is removed. (e) The original B-scan. (f) The de-noised B-scan.

$\phi(x, y, z)$ is initialised according to [16]:

$$\begin{cases} \phi(x,y,z) = -2, & \text{if } (x,y,z) \in \text{choroidal layer} \\ \phi(x,y,z) = 2, & \text{if } (x,y,z) \in \text{background} \\ \phi(x,y,z) = 0, & \text{if } (x,y,z) \in \partial\Omega \end{cases} \quad (4)$$

B. Level Set Method

We use the Level Set Methods (LSM), which has been widely applied to image segmentation [17]–[25], to estimate the posterior choroidal boundary from the shrunken OCT image. The energy functional of our segmentation model is formulated as:

$$E(\phi) = E_M(\phi) + E_E(\phi) + E_R(\phi), \quad (5)$$

The first term E_M is a region-based term, which the Markov Random Field method is used to incorporate the neighbouring pixels with the single pixel likelihood function to smooth and tighten the choroidal boundary and to avoid leakages from the boundary. The second term E_E incorporates the edge information to direct the initial contour to the boundary. Although the edge between the choroid and sclera is indistinct or even invisible at some locations, the edge information is still important in guiding the contour to the desired boundary. Therefore, we incorporated the edge-based information to assist the segmentation. The Geodesic Active Contour model (GAC) [26] based edge term has its regularisation effect. However for this particular problem, the edge information of the data is not clear and the shapes are irregular, so the distance regularisation term is necessary to smooth the boundary and avoid small contours. The last term E_R is a distance regularisation term, which keeps the choroidal layer boundary smooth.

1) Prior Model Construction: According to the initial contour, we set the choroidal area as label 0 and the background as label 1 ($L = \{0, 1\}$). The Gaussian Mixture Model (GMM) is used to model the choroidal layer and background region,

respectively. Given an input 3D image $B = (b_1, ..., b_i, ..., b_N)$, where N is the total number of all pixels. $A = (a_1, ..., a_i, ...a_N)$ ($a_i \in L$) is the corresponding initial label according to the level set function ϕ. It is assumed that the voxel intensity b_i follows a GMM with C components. The parameter set Θ^0 of the initial GMM is learned from A and B by using the Expectation Maximisation (EM) algorithm.

The parameters set $\Theta = \{\theta_l | l \in L\}$ can be expressed as:

$$\theta_l = (\mu_{l,1}, \sigma_{l,1}, \omega_{l,1}), ..., (\mu_{l,C}, \sigma_{l,C}, \omega_{l,C}) \quad (6)$$

The E-step: At the tth iteration, we can obtain the parameters Θ^t, and the conditional expectation can be deduced as:

$$\begin{aligned} Q(\Theta|\Theta^t) &= E_A \left[\ln P(A, B|\Theta) | B, \Theta^t \right] \\ &= \sum_{A \in L} P(A|B, \Theta^t) \ln P(A, B|\Theta) \end{aligned} \quad (7)$$

where L is the set of all possible labels, and $P(A, B|\Theta)$ can be rewritten as:

$$P(A, B|\Theta) = P(A|B)P(B|\Theta) \quad (8)$$

M-step: Next parameter set Θ^{t+1} is estimated through maximising $Q(\Theta|\Theta^t)$:

$$\Theta^{t+1} = \arg\max_{\Theta} Q(\Theta|\Theta^t) \quad (9)$$

The parameters are updated by using $P(l|b_i)$

$$\mu_l^{(t+1)} = \frac{\sum_i P^t(l|b_i)b_i}{\sum_i P^t(l|b_i)}$$

$$(\sigma_l^{(t+1)})^2 = \frac{\sum_i P^t(l|b_i)(b_i - \mu_l^{(t+1)})^2}{\sum_i P^t(l|b_i)} \quad (10)$$

Then, let $\Theta^{t+1} \to \Theta^t$ and repeat from the E-step until it converges.

In previous studies, the GMM parameters are often estimated from a static training process [4], [27], and therefore may be limited to the chosen training set if it does not provide an appropriate coverage of the variation of the data. However, we update the parameters dynamically through the segmentation iterations until the algorithm converges or reaches the maximum iterations to ensure the characteristics of the input data are captured.

2) Region-Based Term: The MRF method has been modified and embedded into the graph cut method as a region based term to segment images [28], [29]. Paragios *et al.* [30] and Zhou *et al.* [20] presented the object tracking method based on level set method with MRF from a moving camera. The MRF has been used for image segmentation for decades and first introduced to segment Brain MR images by Zhang *et al.* [31]. Chen [25] reported the Bayesian risk term based level set method for medical image segmentation. Further extended work [18], [21], [22], [32] improved Chen's method by incorporating the neighbouring pixel information and presented a MRF embedded level set method for 2D image segmentation by using a single Gaussian. Because the intensity inhomogeneity and inconsistent texture in both of the choroidal area and background, it makes the single Gaussian difficult to model the complexity of the problem. Therefore, the GMM is modelled into the MRF method to accurately estimate the choroidal layer. Thisensures the spatial context within the local neighbourhood is incorporated into the model to keep the choroidal layer boundary smooth and to avoid leakages. The region-based energy functional is formulated as:

$$E_M(\phi) = -\nu \int_\Omega \log(P(A|B)) dx dy dz \tag{11}$$

where $\nu \in \mathcal{R}$ is constant coefficients. This term calculates the average of negative log-likelihood of the posterior segmentation probability.

According to the Bayes theorem, $P(A|B)$ can be formulated as:

$$P(A|B) = \frac{P(B|A)P(A)}{P(B)} \tag{12}$$

where $P(B)$ is defined by the image itself and is a constant. Therefore, it can be rewritten as:

$$P(A|B) \propto P(B|A)P(A) \tag{13}$$

where $P(B|A)$ is the conditional segmentation probability, and $P(A)$ is the prior probability.

Based on the conditional independence assumption of b_i, the conditional segmentation probability $P(B|A, \Theta)$ can be expressed as:

$$P(B|A, \Theta) = \prod_{i=0}^{N} P(b_i|a_i, \theta_{a_i}) = \prod_{i=0}^{N} G_{\text{mix}}(b_i; \theta_{a_i})$$

$$= \frac{1}{Z'} \exp(-U(B|A)) \tag{14}$$

The weighted probability of the GMM is:

$$G_{\text{mix}}(b_i; \theta_{a_i}) = \sum_{c=1}^{C} G_{\text{mix}}(b_i; \omega_{a_i,c}, \mu_{a_i,c}, \sigma_{a_i,c})$$

$$= \sum_{c=1}^{C} \omega_{a_i,c} g(b_i; \mu_{a_i,c}, \sigma_{a_i,c})$$

$$= \sum_{c=1}^{C} \frac{\omega_{a_i,c}}{\sqrt{2\pi\sigma_{a_i,c}^2}} \exp\left(-\frac{(b_i - \mu_{a_i,c})^2}{2\sigma_{a_i,c}^2}\right)$$

$$= \sum_{c=1}^{C} \omega_{a_i,c} \exp\left(\frac{-\log(2\pi\sigma_{a_i,c}^2)}{2} + \frac{-(b_i - \mu_{a_i,c})^2}{2\sigma_{a_i,c}^2}\right) \tag{15}$$

According to the Jensen's inequality, if $\sum_{c=1}^{C} \omega_{a_i,c} = 1$, we can conclude that

$$-\log\left(\sum_{c=1}^{C} \omega_{a_i,c} g(b_i; \theta_{a_i,c})\right) \leqslant -\sum_{c=1}^{C} \omega_{a_i,c} \log(g(b_i; \theta_{a_i,c})) \tag{16}$$

It indicates that minimising the right-hand term will lead to the minimisation of the left-hand term. Therefore, the conditional log-likelihood energy function $U(B|A, \Theta)$ can be defined by:

$$U(B|A, \Theta) = \sum_{i=0}^{N} \omega_{a_i} U(b_i|a_i, \Theta)$$

$$= \sum_{i=0}^{N} \sum_{c=1}^{C} \omega_{a_i,c} \left[\frac{(b_i - \mu_{a_i,c})^2}{2\sigma_{a_i,c}^2} + \frac{1}{2}\log(2\pi\sigma_{a_i,c}^2)\right] \tag{17}$$

The prior probability $P(A)$ is defined as:

$$P(A) = P(\phi) = \frac{1}{Z} \exp(-U(\phi)) \tag{18}$$

where the prior energy function $U(\phi)$ is defined as:

$$U(\phi) = \sum_{n \in N_{26}} V_n(\phi) \tag{19}$$

where $V_n(\phi)$ is the clique potential and N_{26} is the set of all possible cliques. The 26-neighborhood system of a voxel $p = (x, y, z)$ is:

$$N_{26} = \{(x \pm 1, y, z), (x, y \pm 1, z), (x, y, z \pm 1),$$

$$(x \pm 1, y \pm 1, z), (x \pm 1, y, z \pm 1),$$

$$(x, y \pm 1, z \pm 1), (x \pm 1, y \pm 1, z \pm 1),\} \tag{20}$$

The clique potential $V_n(\phi)$ is:

$$V_n(\phi_p, \phi_q) = \beta(1 - I_{\phi_p, \phi_q}), \tag{21}$$

where the weight β is defined as $\frac{1}{2\|p-q\|_2}$ and the function I_{ϕ_p, ϕ_q} is:

$$I_{\phi_p, \phi_q} = \begin{cases} 1, & \text{if } \phi_p = \phi_q \\ 0, & \text{if } \phi_p \neq \phi_q \end{cases} \tag{22}$$

Finally, the region-based term can be rewritten as:

$$E_M(\phi) = \nu \int_\Omega \{U(B|A, \Theta) + U(A)\}dxdydz$$

$$= \nu \Big\{ \int_\Omega \{U(B|A, \Theta_0) + U(A)\}H(-\phi)dxdydz$$

$$+ \int_\Omega \{U(B|A, \Theta_1) + U(A)\}H(\phi)dxdydz \Big\} \quad (23)$$

where $H(\phi)$ is the Heaviside function and is defined as:

$$H(\phi) = \begin{cases} 1, & \phi \geqslant 0, \\ 0, & \phi < 0, \end{cases} \quad (24)$$

Compared to other methods [18], [21], [22], our method works more efficiently on 3D volumes with non-uniformity and inconsistent texture by using the GMM instead of a single Gaussian model. The main contribution of this part is that we construct the region-based term by using the GMM based MRF method and embed them into the level set framework.

3) Edge Constrained Term: Although the edge between the choroid and sclera is indistinct or even invisible at some locations, the edge information is still important in guiding the contour to the desired boundary. Therefore, we incorporated the edge-based information to assist the segmentation. The edge constraint term follows the Geodesic Active Contour model [26], and is defined as [16]:

$$E_E(\phi) = \lambda L_g(\phi) + \alpha A_g(\phi), \quad (25)$$

where $\lambda > 0$ and $\alpha \in \mathcal{R}$ are constant coefficients, which are set to 5 and -3 respectively in our experiments. The energy functionals $L_g(\phi)$ and $A_g(\phi)$ are formulated as:

$$L_g(\phi) \approx \int_\Omega g\delta(\phi(x, y, z))|\nabla\phi(x, y, z)|dxdydz \quad (26)$$

$$A_g(\phi) \approx \int_\Omega gH(-\phi(x, y, z))dxdydz \quad (27)$$

where g, H_ϵ, δ_ϵ are the edge indicator function, the Heaviside function and Dirac delta function, respectively. The edge indicator function is defined by:

$$g \approx \frac{1}{1 + |\nabla G * I(x, y, z)|} \quad (28)$$

where G is the Gaussian kernel, the kernel size of the Gaussian is set to $13 \times 13 \times 13$ in our experiments. The indicator is used to smooth the image and reduce the noise through the convolution. In addition, the Dirac delta function $\delta(\phi)$ is:

$$\delta(\phi) = \frac{d}{d\phi}H(\phi) \quad (29)$$

The first term $L_g(\phi)$ in (25) calculates the line integral of the edge indicator function g along the zero level set contour of ϕ with the Dirac delta function δ_ϵ. When the zero level set of ϕ as a contour is parameterised as C: $[0, 1] \rightarrow \Omega$, $L_g(\phi)$ can be rewritten as $\int_0^1 g(|\nabla I(C(s))|)|(C(s))|ds$. This term $\int_0^1 g(|\nabla I(C(s))|)|(C(s))|ds$ was first introduced by Caselles

et al. [26], where $g(|\nabla I(C(s))|)|$ contains the boundary information of the object. The energy of this term $L_g(\phi)$ is minimised when the level set function ϕ is close to the target boundary of the object.

A weighted area of the region $\Omega_\phi^- \approx \phi(X) < 0$ is calculated by the second term $A_g(\phi)$. When $g(x) = 1$ as a special case, the term $A_g(\phi)$ computes the area within the contour Ω_ϕ^-. $A_g(\phi)$ is applied to speed up the motion of the level set function ϕ to the desired object boundary in the evolution process, especially when the initial contour is located far away from the target boundary of the object. The level set function ϕ is negative inside the zero level contour and positive outside the zero level contour. The coefficient α for the weighted area term should be positive when the initial contour is located outside the object, so that the zero level contour will shrink to the target boundary in the level set evolution. Otherwise, the coefficient α should be negative when the initial contour is located inside of the initial contour, so that the zero level contour will expand to the target boundary in the level set evolution. When the edge indicator function $g(x)$ is close to the object boundary, this weighted area term $A_g(\phi)$ will slow down the shrinking or expanding of the zero level contour.

4) Distance regularisation Term: In order to maintain the boundary of the choroid, the distance regularisation term is added to the energy functional. The regularisation term in the energy functional is:

$$E_R(\phi) = \lambda_R E_R(\phi) \quad (30)$$

where λ_R is a positive valued parameter and is set to 1. $E_R(\phi)$ computes the contour length of the zero level set ϕ to smooth the boundary of the choroidal area. The equation of $E_R(\phi)$ is defined by:

$$E_R(\phi) = \int_\Omega \delta(\phi(x, y, z))|\nabla\phi(x, y, z)|dxdydz \quad (31)$$

C. Partial Differential Equation based Energy Minimisation

The energy terms defined by (23), (25) and (30) are substituted into (5), and our energy model of $E(\phi)$ can be rewritten as:

$$E(\phi) = \nu \Big\{ \int_\Omega \{U(B|A, \Theta_0) + U(A)\}H(-\phi)dxdydz$$

$$+ \int_\Omega \{U(B|A, \Theta_1) + U(A)\}H(\phi)dxdydz \Big\}$$

$$+ \lambda \int_\Omega g\delta(\phi)|\nabla\phi|dxdydz + \alpha \int_\Omega gH(-\phi)dxdydz$$

$$+ \lambda_R \int_\Omega \delta(\phi)|\nabla\phi|dxdydz \quad (32)$$

According to the Euler-Lagrange differential equation [33], the energy minimisation problem $\frac{\partial E(\phi)}{\partial \phi}$ can be reformulated as:

$$\frac{\partial\phi}{\partial t} = -\frac{\partial E(\phi)}{\partial \phi} \quad (33)$$

and the corresponding gradient flow equation is defined as:

$$\frac{\partial \phi}{\partial t} = \nu\{-\{U(B|A, \Theta_0) + U(A)\}$$
$$+ \{U(B|A, \Theta_1) + U(A)\}\}\delta(\phi)$$
$$+ \left\{\lambda\left(\nabla g|\nabla\phi| + g\,\text{div}\left(\frac{\nabla\phi}{|\nabla\phi|}\right) + \alpha g\right\}\delta(\phi)$$
$$+ \lambda_R \text{div}\left(\frac{\nabla\phi}{|\nabla\phi|}\right) \quad (34)$$

where $div(\cdot)$ is the divergence operator, which is used to calculate the curvature of the evolving curve by using the spatial derivatives ϕ up to the second order.

Finally, the level set equation can be reformed as:

$$\phi(t+1) = \phi(t) + \nabla t\{\nu\{-\{U(B|A, \Theta_0) + U(A)\}$$
$$+ \{U(B|A, \Theta_1) + U(A)\}\}\delta(\phi)$$
$$+ \left\{\lambda\left(\nabla g|\nabla\phi| + g\,\text{div}\left(\frac{\nabla\phi}{|\nabla\phi|}\right) + \alpha g\}\delta(\phi)\right.$$
$$+ \lambda_R \text{div}\left(\frac{\nabla\phi}{|\nabla\phi|}\right)\} \quad (35)$$

where ∇t is the time step, and t is the temporal index.

In order to reduce the computational cost of a level set method, the narrowband around the zero level set is updated instead of ϕ in the full image domain. The Gradient Vector Flow (GVF) method [34] is used to construct the narrowband around the zero level set. The GVF method preserves a diffusion of the gradient feature information and avoids the leakage of the boundary. According to [34], the vector flow field $\vec{V}(x, y, z) = [u(x, y, z), v(x, y, z), w(x, y, z)]$ is defined to minimise an energy function as follows:

$$e = \int \mu|\nabla\vec{V}|^2 + |\nabla\vec{f}|^2|\vec{V} - \nabla\vec{f}|dxdydz \quad (36)$$

where μ is a regularisation parameter, f is the edge map of the Heaviside function H, and $V = \nabla f$.

$$f = G_\sigma(x, y, z) * H(\phi(x, y, z)) \quad (37)$$

where $G_\sigma(x, y, z)$ is a three-dimensional Gaussian function with standard deviation σ. The first term is the smoothing term and the second term is the data term, which is minimised when $V = \nabla f$.

The numerical implementation of this energy function problem is formulated as:

$$u^{t+1}(x, y, z) = \mu\nabla^2 u^t(x, y, z) - \left[u^t(x, y, z) - f_x(x, y, z)\right]$$
$$\left[f_x(x, y, z)^2 + f_y(x, y, z)^2 + f_z(x, y, z)^2\right] \quad (38)$$

$$v^{t+1}(x, y, z) = \mu\nabla^2 v^t(x, y, z) - \left[v^t(x, y, z) - f_y(x, y, z)\right]$$
$$\left[f_x(x, y, z)^2 + f_y(x, y, z)^2 + f_z(x, y, z)^2\right] \quad (39)$$

$$w^{t+1}(x, y, z) = \mu\nabla^2 w^t(x, y, z) - \left[w^t(x, y, z) - f_z(x, y, z)\right]$$
$$\left[f_x(x, y, z)^2 + f_y(x, y, z)^2 + f_z(x, y, z)^2\right] \quad (40)$$

Finally, in order to create a wider narrowband, the Dirac delta function $\delta(\phi)$ can be rewritten as:

$$\delta(\phi) = u(x, y, z) + v(x, y, z) + w(x, y, z) \quad (41)$$

It is important to note that the GVF has been used for the first time to estimate a more comprehensive narrowband around the zero level set. It can estimate the vertical direction narrowband more efficiently than the sparse field method [23]. Furthermore, the speed of the GVF is faster than the sparse field method because this method updates the whole volume while the GVF just updates the narrowband only. The computational cost depends on the iteration number of the GVF. So the higher the iteration number, the faster the speed can be achieved, however it may over locate the choroidal boundary. The iteration number is set to 15 in our experiments.

III. EXPERIMENTS

The dataset of the macular images were collected at Beijing Tongren Hospital, China by using the volume scan mode with the Swept Source OCT (DRI OCT Atlantis, Topcon, Tokyo, Japan). The data collection was undertaken in accordance with the organisation's research ethics regulations and was approved by the local ethics committee. The dataset includes 30 3D OCT scans from 30 healthy subjects aged between 20 to 85 years. The images are centred at the macula region. The image size is $256 \times 512 \times 992$ with 16 bits per pixel and a digital axial resolution of 3.9 μm per pixel. This imaging protocol has been commonly used to diagnose retinal diseases. 20 B-scans of each volume images were uniformly selected and manually labelled along the outmost edges of the choroidal vessels. Then a simple linear interpolation between two consecutive labelled B-scans was performed to provide the boundary points on the unlabelled B-scans in between. This is served as the ground truth in our experiments. The process was conducted under the supervision of clinical experts. Because the variation between slices is relatively small around the macula area, this interpolated ground truth has been confirmed as appropriate by the experts.

It is important to note that choroidal thickness measurements are highly variable in practice owing to the lack of a standardised definition of the choroidal-scleral junction and the often obscure imaging appearance in this region [35]. In our experiments the outmost edges of the choroidal vessels are labelled as the posterior choroidal boundary.

The proposed method (A) was evaluated on the above dataset against a number of other methods. These include two variants
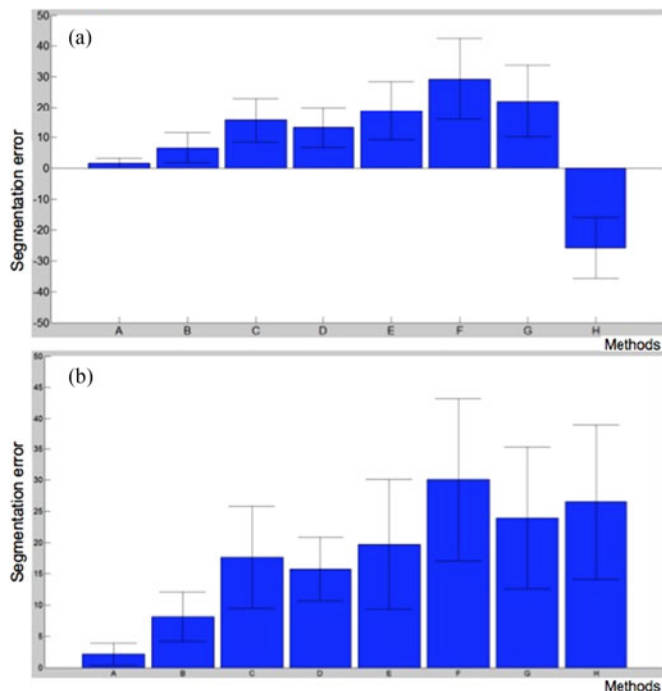
Fig. 3. The mean segmentation error of the posterior choroidal layer boundary by different methods, including the proposed method (A), the Level Set Method with single Gaussian and MRF (B), the proposed method without MRF (C), MRF (D), Graph Cut method (E), Chan-Vese LSM (F), Canny Edge detection (G), and K-means algorithm (H). (a) The mean signed mean difference between the ground truth and the segmentation results and the standard deviation. (b) The mean unsigned difference and the standard deviation.

Fig. 4. The mean Dice's coefficient of the choroidal layer between each individual method and the ground truth. The methods (A-H) are lablled in the same way as in Fig. 3.

of the proposed method: the Level Set Method with single Gaussian and MRF (B), the Level Set Method without the MRF term (C), the conventional segmentation methods MRF (D) [36], the Graph Cut method (E) [37], the Chan-Vese Level Set Method (F) [38], the Canny edge detector (G) [36], and the K-means algorithm (H) [36]. In general the selection of evaluation methods covers the state-of-the-art as reviewed in Section I, but it is important to note that our implementation may be different from the original studies.

Two common metrics of error used to evaluate the performance of our segmentation are the signed and unsigned mean difference. Fig. 3 compares the mean signed and unsigned mean and standard deviation (sd) between the ground truth and the segmentation results from different methods. For the proposed method, the mean signed difference is 1.59 ± 1.65 pixels and the mean unsigned difference is 2.17 ± 1.77 pixels.

Also, Dice's coefficient was used to measure the similarity between the segmentation results and the ground truth. The coefficient is defined as:

$$s = \frac{2|A \bigcap B|}{|A| + |B|} \qquad (42)$$

where A and B are the segmented choroidal region and the manual labelled choroidal region, respectively. The mean Dice's coefficient of the dataset was calculated and compared with different methods including the proposed method in Fig. 4. For
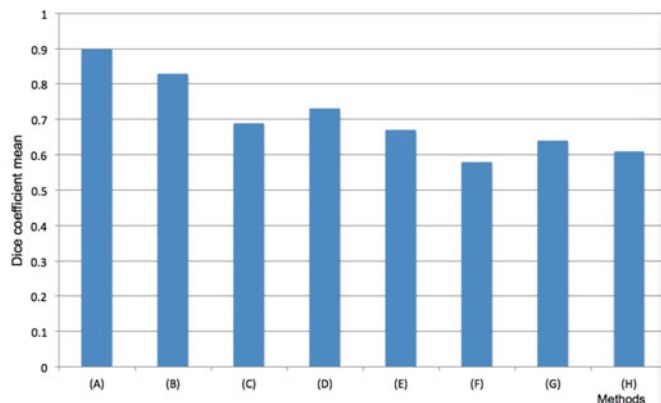
the proposed method, the mean Dice's coefficient of 30 volume images in the dataset is 90% with the standard deviation around 4%. The best Dice's coefficient value is 95% in the dataset, while the worst performance is 86%.

As shown in Figs. 3 and 4, the proposed method (A) achieved the best segmentation accuracy in terms of the mean differences and the Dice's coefficient. The proposed method with single Gaussian and MRF (B) performed well but is slightly inferior to (A), while the proposed methods without MRF (C) performed much worse than (A) and (B). This indicates that the region term defined by the MRF is a crucial part of the model. Among the other methods, the MRF performed the best but still only comparable to (C) and much inferior to (A). As expected, the simple methods such as the Canny edge detector (G) and the K-means algorithm (H) did not perform well as they do not have the intrinsic mechanism to handle the challenges of the problem discussed earlier. Also, the Chan-Vese method (F) did not provide as good results as the other methods, because it cannot deal effectively with inhomogeneous regions.

Fig. 5 shows the segmentation results of the posterior choroidal boundary on a sample of 12 B-scans. For clarity of illustration, only three sets of results from the proposed method (the best in terms of the metrics set above, in black), the proposed method without MRF (the second best, in red), and the Chan-Vese method (the worst, in yellow) are shown here together with the ground truth (in purple). The thickness map of the choroidal layer in the same volume image is estimated and displayed in Fig. 6 according to [39].

A number of parameters are required to be set in the proposed approach. We have used a simple trial-and error method for this. In our experiments, inappropriate parameter settings did affect the segmentation performance and occasionally failed to produce the desired results. However, we believe this is a common issue for all the level set based methods.

The proposed method is implemented on MATLAB. The average computational time for an image is 43.29 minutes on a PC with a 3.3 GHz Intel Core i5-2500 CPU and 8GB RAM. Similar to other iterative segmentation methods, slow computation is
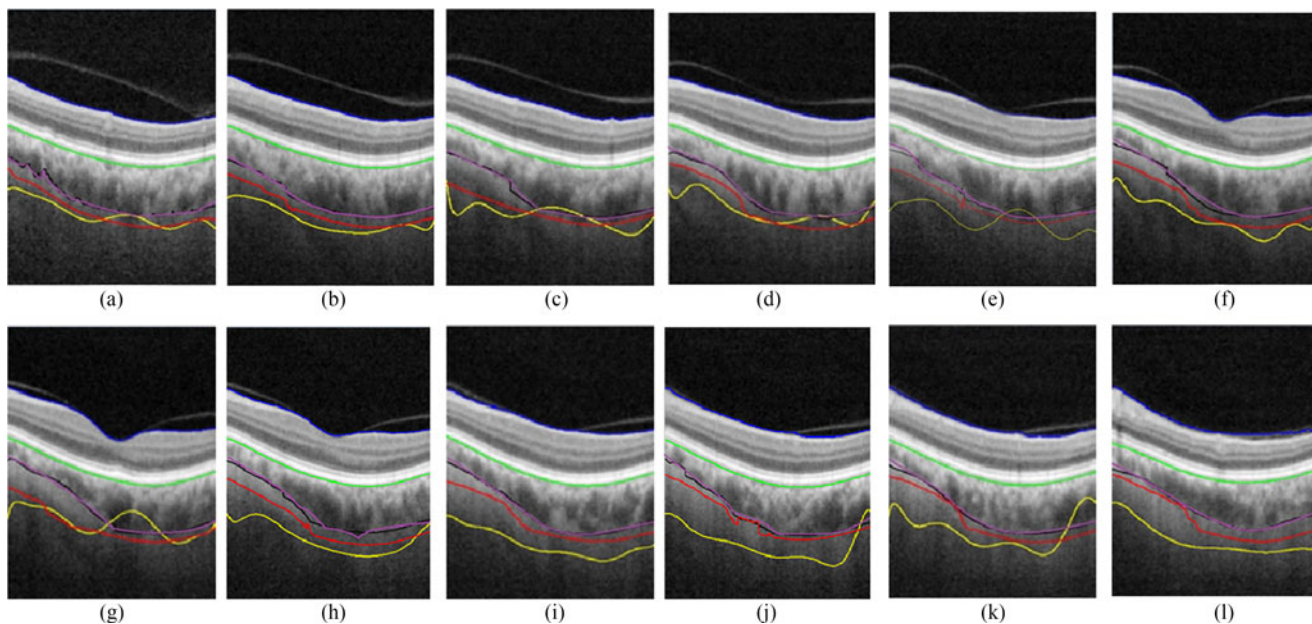
Fig. 5. Examples of the choroid layer segmented. The segmentation result by the proposed method is in black, the ground truth in purple, the proposed method without MRF (C) in red, and the Chan-Vese LSM (F) in yellow, while the upper choroidal boundary is marked in green and the upper Nerve Fiber Layer (NFL) in blue. (a)–(l) are the results from the 10th, 30th, 50th, 70th, 90th, 110th, 130th, 150th, 170th, 190th, 210th, 230th B-scans the image respectively.
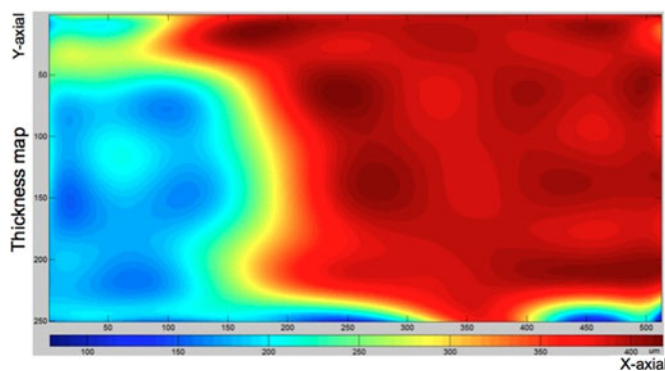

Fig. 6. Choroidal thickness map for the same image as in Fig. 5.

one of the limitations of our method. Also, the MATLAB is not considered as one of the fastest platforms, so the computational time can be improved if implemented by other platforms such as C++ or Graphic Programming Units (GPU).

IV. CONCLUSIONS AND FUTURE WORK

Segmenting the choroidal layer from the 3D OCT macular images is challenging in that (1) the contrast between the choroid and sclera is weak, (2) the intensity of this layer is inhomogeneous and the texture of this layer is inconsistent because of the blood vessels inside the layer, and (3) appearance between the choroid and the sclera is indistinct.

In this study, we have presented an automatic choroidal layer segmentation method for 3D OCT macular images. In the first step, we use the anisotropic diffusion filter to remove the speckle noise and enhance the contrast between the choroid and sclera.

Afterward, the zero contour function is initialised according to the prior information from the choroidal layer. Based on the zero contour, the GMM is used to model both the choroidal area and the background. The region-based term is embedded into the level set energy function by using the Markov Random Field to model the appearance of pixels in their local neighbourhood. Furthermore, the edge constraint term and distance regularisation term are included into the level set function to direct the contour to the desired boundary and to avoid small and irregular contours.

The choroid layer segmentation method has been evaluated against a number of alternative methods on a dataset with manually labelled ground truth. The experimental results show that the proposed method has the following advantages:(1) The MRF term with GMM adequately models the intensity inhomogeneity of the choroid. (2) The neighbouring information is modelled into the region based term to avoid small regions and smooth the boundary. (3) The edge constraint term is embedded into the energy function to direct the contour to the desired boundary. (4) The distance regularisation term is modelled into the energy function to avoid small and irregular contours.

The contributions of the work are: (1) The region based term, incorporating the neighbouring pixel information with the single pixel log-likelihood function by using the Markov Random Field, is modelled into the level set method; (2) The GMM is constructed and updated at each level set iteration, instead of learned offline from a fixed training set;(3) Finally, the GVF method is used to estimate more comprehensive narrowband around the zero level set to increase the speed of the segmentation.

In future work, we will investigate the correlation between the choroidal thickness map and choroidal diseases. We also will

try to segment and reconstruct the blood vessels in the choroidal layer and produce 3D vascular structures for diagnosing the choroidal diseases.

REFERENCES

[1] A. Bill, G. Sperber, and K. Ujiie, "Physiology of the choroidal vascular bed," *Int. Ophthalmology*, vol. 6, no. 2, pp. 101–107, 1983.

[2] D. L. Nickla and J. Wallman, "The multifunctional choroid," *Progress Retinal Eye Res.*, vol. 29, no. 2, pp. 144–168, 2010.

[3] C. V. Regatieri, L. Branchini, J. G. Fujimoto, and J. S. Duker, "Choroidal imaging using spectral-domain optical coherence tomography," *Retina*, vol. 32, no. 5, pp. 865–876, 2012.

[4] V. Kajić, M. Esmaeelpour, B. Považay, D. Marshall, P. L. Rosin, and W. Drexler, "Automated choroidal segmentation of 1060 nm OCT in healthy and pathologic eyes using a statistical model," *Biomed. Opt. Express*, vol. 3, no. 1, pp. 86–103, 2012.

[5] Z. Hu, X. Wu, Y. Ouyang, Y. Ouyang, and S. R. Sadda, "Semiauto- mated segmentation of the choroid in spectral-domain optical coherence tomography volume scans," *Investigative Ophthalmology Vis. Sci.*, vol. 54, no. 3, pp. 1722–1729, 2013.

[6] J. Tian, P. Marziliano, M. Baskaran, T. A. Tun, and T. Aung, "Automatic segmentation of the choroid in enhanced depth imaging optical coherence tomography images," *Biomed. Opt. Express*, vol. 4, no. 3, pp. 397–411, 2013.

[7] D. Alonso-Caneiro, S. A. Read, and M. J. Collins, "Automatic segmen- tation of choroidal thickness in optical coherence tomography," *Biomed. Opt. Express*, vol. 4, no. 12, pp. 2795–2812, 2013.

[8] H. Danesh, R. Kafieh, H. Rabbani, and F. Hajizadeh, "Segmentation of choroidal boundary in enhanced depth imaging OCTs using a multires- olution texture based modeling in graph cuts," *Comput. Math. Methods Med.*, vol. 2014, 2014, Art. no. 479268.

[9] M. Esmaeelpour *et al.*, "Choroidal haller's and sattler's layer thickness measurement using 3-dimensional 1060-nm optical coherence tomogra- phy," *PloS One*, vol. 9, no. 6, 2014, Art. no. e99690.

[10] F. Rossant, I. Ghorbel, I. Bloch, M. Paques, and S. Tick, "Automated segmentation of retinal layers in OCT imaging and derived ophthalmic measures," in *Proc. 2009 IEEE Int. Symp. Biomed. Imag., From Nano Macro*, pp. 1370–1373, 2009.

[11] I. Ghorbel, F. Rossant, I. Bloch, S. Tick, and M. Paques, "Automated segmentation of macular layers in OCT images and quantitative evaluation of performances," *Pattern Recognit.*, vol. 44, no. 8, pp. 1590–1603, 2011.

[12] C. Wang *et al.*, "Segmentation of intra-retinal layers in 3D optic nerve head images," in *Proc. Int. Conf. Image Graph.*, 2015, pp. 321–332.

[13] R. Kafieh, H. Rabbani, and S. Kermani, "A review of algorithms for seg- mentation of optical coherence tomography from retina," *J Med. Signals Sensor*, vol. 3, no. 1, pp. 45–60, 2013.

[14] G. Gerig, O. Kubler, R. Kikinis, and F. A. Jolesz, "Nonlinear anisotropic filtering of MRI data," *IEEE Trans. Med. Imag.*, vol. 11, no. 2, pp. 221– 232, Jun. 1992.

[15] C. Wang, Y. Wang, D. Kaba, Z. Wang, X. Liu, and Y. Li, "Automated layer segmentation of 3D macular images using hybrid methods," in *Proc. Int. Conf. Image Graph.*, 2015, pp. 614–628.

[16] C. Li, C. Xu, C. Gui, and M. D. Fox, "Distance regularized level set evolution and its application to image segmentation," *IEEE Trans. Image Process.*, vol. 19, no. 12, pp. 3243–3254, Dec. 2010.

[17] X. Yang, X. Gao, J. Li, and B. Han, "A shape-initialized and intensity- adaptive level set method for auroral oval segmentation," *Inf. Sci.*, vol. 277, pp. 794–807, 2014.

[18] X. Yang, X. Gao, D. Tao, X. Li, and J. Li, "An efficient MRF embedded level set method for image segmentation," *IEEE Trans. Image Process.*, vol. 24, no. 1, pp. 9–21, Jan. 2015.

[19] X. Yang, X. Gao, D. Tao, and X. Li, "Improving level set method for fast auroral oval segmentation," *IEEE Trans. Image Process.*, vol. 23, no. 7, pp. 2854–2865, Jul. 2014.

[20] X. Zhou, W. Hu, Y. Chen, and W. Hu, "Markov random field modeled level sets method for object tracking with moving cameras," in *Asian Conf. Computer Vision*, pp. 832–842, 2007.

[21] Z. Shahvaran, K. Kazemi, M. S. Helfroush, N. Jafarian, and N. Noorizadeh, "Variational level set combined with Markov random field modeling for simultaneous intensity non-uniformity correction and segmentation of mr images," *J. Neurosci. Methods*, vol. 209, no. 2, pp. 280–289, 2012.

[22] Z. Shahvaran, K. Kazemi, M. S. Helfroush, and N. Jafarian, "Region- based active contour model based on Markov random field to segment images with intensity non-uniformity and noise," *J. Med. Signals Sensors*, vol. 2, no. 1, pp. 17–24, 2012.

[23] A. C. Jalba, W. J. van der Laan, and J. B. Roerdink, "Fast sparse level sets on graphics hardware," *IEEE Trans. Vis. Comput. Graphics*, vol. 19, no. 1, pp. 30–44, Jan. 2013.

[24] C. Li, R. Huang, Z. Ding, J. C. Gatenby, D. N. Metaxas, and J. C. Gore, "A level set method for image segmentation in the presence of intensity inhomogeneities with application to MRI," *IEEE Trans. Image Process.*, vol. 20, no. 7, pp. 2007–2016, Jul. 2011.

[25] Y.-T. Chen, "A level set method based on the Bayesian risk for medical image segmentation," *Pattern Recognit.*, vol. 43, no. 11, pp. 3699–3711, 2010.

[26] V. Caselles, R. Kimmel, and G. Sapiro, "Geodesic active contours," *Int. J. Comput. Vis.*, vol. 22, no. 1, pp. 61–79, 1997.

[27] P. P. Srinivasan, S. J. Heflin, J. A. Izatt, V. Y. Arshavsky, and S. Farsiu, "Automatic segmentation of up to ten layer boundaries in SD-OCT images of the mouse retina with and without missing layers due to pathology," *Biomed. Opt. Express*, vol. 5, no. 2, pp. 348–365, 2014.

[28] Y. Boykov and V. Kolmogorov, "Computing geodesics and minimal sur- faces via graph cuts," in *Proc. 9th IEEE Int. Conf. Comput. Vis.*, 2003, pp. 26–33.

[29] I. B. Ben Ayed, K. Punithakumar, and S. Li, "Distribution matching with the Bhattacharyya similarity: A bound optimization framework," *IEEE Trans. Pattern Anal. Mach. Learn. Intell.*, vol. 37, no. 9, pp. 1777–1791, Sep. 2005.

[30] N. Paragios and R. Deriche, "Unifying boundary and region-based infor- mation for geodesic active tracking," in *Proc. IEEE Comput. Soc. Conf. Comput. Vis. Pattern Recognit.*, vol. 2, 1999, pp. 300–305.

[31] Y. Zhang, M. Brady, and S. Smith, "Segmentation of brain mr im- ages through a hidden markov random field model and the expectation- maximization algorithm," *IEEE Trans. Med. Imag.*, vol. 20, no. 1, pp. 45–57, Jan. 2001.

[32] M. S. Allili and D. Ziou, "An automatic segmentation combining mixture analysis and adaptive region information: A level set approach," in *Proc. 2nd Can. Conf. Comput. Robot Vis. 2005*, 2005, pp. 73–80.

[33] G. Aubert and P. Kornprobst, *Mathematical Problems in Image Pro- cessing: Partial Differential Equations and the Calculus of Variations*, vol. 147. New York, NY, USA: Springer-Verlag, 2006.

[34] J. Prince, "Gradient vector flow: A new external forces for snakes," *IEEE Trans. Image Process.*, vol. 7, no. 3, pp. 359–369, Mar. 1998.

[35] V. S. Vuong, E. Moisseiev, D. Cunefare, S. Farsiu, A. Moshiri, and G. Yiu, "Repeatability of choroidal thickness measurements on enhanced depth imaging optical coherence tomography using different posterior boundaries," *Amer. J. Ophthalmology*, vol. 169, pp. 104–112, 2016.

[36] R. Szeliski, *Computer Vision: Algorithms and Applications*. New York, NY, USA: Springer-Verlag, 2010.

[37] Y. Y. Boykov and M.-P. Jolly, "Interactive graph cuts for optimal boundary & region segmentation of objects in ND images," in *Proc. 8th IEEE Int. Conf. Comput. Vis.*, 2001, vol. 1, pp. 105–112.

[38] T. F. Chan, B. Y. Sandberg, and L. A. Vese, "Active contours without edges for vector-valued images," *J. Vis. Commun. Image Represent.*, vol. 11, no. 2, pp. 130–141, 2000.

[39] D. Alonso-Caneiro, S. A. Read, S. J. Vincent, M. J. Collins, and M. Wojtkowski, "Tissue thickness calculation in ocular optical coherence tomography," *Biomed. Opt. Express*, vol. 7, no. 2, pp. 629–645, 2016.

Authors' photographs and biographies not available at the time of publication.